In#Plane Direct#Write Assembly of Iridescent Colloidal Crystals

DOI: 10.1002/((please add manuscript number))
Article type: Communication

In-Plane Direct-Write Assembly of Iridescent Colloidal Crystals

*Alvin T. L. Tan, Sara Nagelberg, Elizabeth Chang-Davidson, Joel Tan, Joel K. W. Yang, Mathias Kolle, A. John Hart**

A. T. L. Tan
Department of Materials Science and Engineering
Massachusetts Institute of Technology
77 Massachusetts Ave, Cambridge, MA 02139, USA

S. Nagelberg, E. Chang-Davidson, Prof. M. Kolle, Prof. A. J. Hart
Department of Mechanical Engineering
Massachusetts Institute of Technology
77 Massachusetts Ave, Cambridge, MA 02139, USA
E-mail: ajhart@mit.edu

J. Tan, Prof. J. K. W. Yang
Pillar of Engineering Product Development
Singapore University of Technology and Design
8 Somapah Road, 487372, Singapore

Keywords: colloids, self-assembly, structural color, additive manufacturing, nanoparticles

Abstract

Materials made by directed self-assembly of colloids can exhibit a rich spectrum of optical phenomena, including photonic bandgaps, coherent scattering, collective plasmonic resonance, and wave guiding. The assembly of colloidal particles with spatial selectivity is critical for studying these phenomena and for practical device fabrication. While there are well-established techniques for patterning colloidal crystals, these often require multiple steps including the fabrication of a physical template for masking, etching, stamping, or directing de-wetting. Here, we present the direct-writing of colloidal suspensions as a technique for fabrication of iridescent colloidal crystals in arbitrary two-dimensional patterns. Leveraging the principles of convective assembly, the process can be optimized for high writing speeds (~600 μm/s) at mild process temperature (30 °C) while maintaining long-range (cm-scale) order in the colloidal crystals. The crystals exhibit structural color by grating diffraction, and

analysis of diffraction allows particle size, relative grain size and grain orientation to be deduced. We present observations about the effect of write trajectory on particle ordering, and provide insights for developing 3-D printing techniques for colloidal crystals via layer-wise sintering.

Main Text

Nature is replete with instances of hierarchically structured materials that create visually stunning appearances. For example, peacock feathers, butterfly wings, and beetle shells are structured on the nano-, meso-, and macro-scales, resulting in iridescence and structural color.[1–3] There is also much scientific interest and commercial value in creating similarly structured man-made materials for applications including photonic devices and visual displays.

These and other technology needs require materials fabrication techniques that provide control of material structure over multiple length scales. Self-assembly provides a convenient means for controlling material structure from the bottom up, and there has been substantial research on convective self-assembly of colloidal particles into photonic crystals, including seminal work by Vlasov[4] and others.[5–8] Patterned colloidal crystals have been created for photonic devices and sensing applications.[9–11] However, these techniques often require the prefabrication of templates or masks, and lithographic etching,[6,12] especially when spatial control of the material is required. An alternate approach would be to print colloidal particles directly onto the substrate from a digital template so that steps such as template fabrication, masking, and etching, can be omitted. Printing from a digital template can be done with inkjet printing, where droplets 20 to 50 μm in diameter are ejected on-demand from microscopic nozzles.[13–16] However, the size of the droplet limits the grain sizes in the resulting colloidal crystal, resulting in weak structural color.[17] Moreover, most inkjet printing techniques require colloidal particle sizes to be limited from 50 to 300 nm for smooth printing,[16,18] and printing larger particles presents nozzle clogging issues.

The combination of direct-write 3D printing with the principle of self-assembly is a potential means to create new hierarchically-ordered materials. For instance, by dispensing a colloidal solution onto a temperature-controlled substrate and coordinating the rate of crystal growth with the retraction of the substrate, it is possible to fabricate colloidal crystals into specific shapes, such as vertical pillars and helices.[19] Here, we extend this technique to the more general case of planar direct-write self-assembly, where evaporation-induced assembly of colloidal particles is guided by the moving meniscus traced by a motorized, liquid-dispensing needle. We show that direct-write self-assembly can build high-quality iridescent colloidal crystals in arbitrary patterns predetermined by a digital template.

Direct-write assembly is performed by the scheme shown in **Figure 1**a. A substrate, typically a piece of silicon wafer or glass, is mounted onto a temperature-controlled (30 °C) precision motion stage with a dispensing needle positioned slightly above the substrate. An aqueous suspension of polystyrene particles (diameter D = 746 nm) is dispensed through the needle and contacts the substrate, forming a liquid meniscus between the needle and the substrate. Unlike slurry inks used in direct ink writing,[20,21] the concentration of the particles is low, and therefore the flow properties of the suspension is similar to the solvent (i.e. water). The substrate is then moved laterally by the stage, while maintaining the gap between the substrate and the needle. As the substrate moves, particles are transported to the trailing edge of the meniscus by an evaporation-induced flux. The particles are then compacted into a colloidal crystal at the trailing edge of the meniscus. Therefore, a crystal can be written by relative motion of the needle over the stage at a velocity matching the approximate rate of crystal growth. An optical image of an exemplary colloidal crystal is shown in Figure 1c. By this method, the trajectory of crystal growth can be influenced by multi-axial stage motion. As an example, Figure 1b shows a serpentine-shaped crystal which appears iridescent to the naked eye, made by coordinated in-plane motion of the stage beneath the needle.

For the purpose of studying the rate of crystal growth, we move the stage in a single direction at a constant speed, denoted as the write speed. The layer thickness of the colloidal crystal can be identified by its thin film interference colors.[22,23] In Figure 1c, blue regions correspond to particle monolayers, green regions correspond to bilayers, and the brown regions correspond to 3 or more layers of particles. We observe that the edge of the crystal is thicker than the middle, a result of outward capillary flow towards the contact line of the meniscus. However, the thickness of the middle region is uniform and can be controlled by the write speed, as will be discussed in detail later. Scanning electron microscopy (SEM) imaging confirms the presence of multiple layers of particles at the edge (Figure 1d) and a uniform crystal thickness in the middle region. In the middle region, the particles are hexagonally packed, albeit with typical crystal defects such as vacancies and dislocations.

The key to continuous direct-write self-assembly of colloidal crystals is matching the write speed to the rate of crystal growth determined by evaporative flux from the trailing meniscus. We can approximate the rate of crystal growth at the trailing end of the meniscus to be that of other convective assembly techniques such as dip-coating and blade-casting. By considering the balance of the rate of crystal growth with the flux of water and particles transported to the crystal growth front, Dimitrov and Nagayama[24] proposed the following equation to calculate the rate of crystal growth v_c:

$$v_c = \frac{\beta l j_e \varphi}{h(1-\varepsilon)(1-\varphi)} \tag{1}$$

Here, h is the height of the crystal, ε its porosity, and φ is the volume fraction of particles in suspension, as depicted in **Figure 2**a. Further, l is a characteristic evaporation length, j_e is the water evaporation flux, and β is an interaction parameter between 0 and 1, where $\beta = 1$ corresponds to complete entrainment of particles by water flux. A particle monolayer is denoted by $h = D$. By replacing the term $\beta l j_e$ with an experimentally fitted parameter K, as previously demonstrated by Prevo and Velev,[25] we can create an operational phase diagram which maps the relationship between experimental variables and crystallinity of the deposited particles. From a series of experiments at different write speeds v and feedstock particle concentrations φ, we identified disordered, ordered, and sub-monolayer phases, as plotted in Figure 2b. The curve delineates the rate of crystal growth for a monolayer according to Equation 1, with $\varepsilon = 0.605$ (corresponding to hexagonal close packing) and $K = 8 \times 10^4$ m^2/s. Below this line, ordered phases of at least single-particle thickness are obtained, such as shown in Figure 2d. Above the line, the write speed v exceeds the rate of crystal growth v_c, resulting in a sub-monolayer deposit, such as shown Figure 2e. Additionally, at very low speeds, the particles are deposited as disordered aggregates, such as shown in Figure 2c.

This information serves as a practical guide for high throughput direct-write self-assembly. As a case in point, the typical as-received concentration of commercial colloidal particles is $\varphi = 0.025$, which requires a write speed of ~50 µm/s for the crystalline phase. However, by simply increasing the concentration of particles to $\varphi = 0.2$ via centrifugation and decanting, the concentrated particle suspension can then be used to boost write speed by an order of magnitude to ~600 µm/s.

By motorized stage motion, a colloidal crystal can be directly patterned using a digital template (e.g., starting with a vector graphic, Figure S1), without the need for further process steps such as etching. The colloid suspension is dispensed at a constant rate while translating the stage according to the script, resulting in a patterned colloidal crystal in the shape of the vector graphic, as shown in **Figure 3**.

The general iridescence visible throughout the colloidal crystal indicates a high degree of crystallinity. Conversely, the small regions that lack iridescence indicate lack of particle order. Specifically, these regions occur where there was a turn or overlap in the toolpath, suggesting that the toolpath trajectory can have a strong influence on self-assembly. Moreover, the local curvature of the toolpath affects order, and the limiting cases are revealed in Figure 3 i, iii and iv. In the limit of a straight line (Figure 3 iii) or wide arc (Figure 3 i), crystallinity is maintained. In contrast, in the limit of a sharp 90 ° turn, a white patch appears on the inside of the turn which indicates a region of disorder. Thus, the appearance of iridescence provides visual feedback on the degree of order or disorder of the colloidal assembly.

Next, we performed a series of experiments with different tool path curvatures. We denote the inner radius of curvature as R and the width of the colloidal trail as W (Figure 3c). Micrographs shown in Figure 3c-f depict colloidal trails with progressively smaller R, yet constant W (governed by the needle diameter). In general, as R decreases relative to W, the deposit of particles on the inside of the turn becomes thicker and eventually becomes disordered when $R < W$. This observation is in general agreement with the phase diagram (Figure 2b), which shows that slow write speeds lead to disordered deposits. The deposition rate of particles relative to the local tangential velocity is inversely proportional to the local curvature of the path. In the experimental conditions for Figure 3f, the volume fraction of particles is $\varphi = 0.05$ and the tangential velocity at the middle of the tool path is v_1 = 146 µm/s. The radius of curvature at the middle of the toolpath is R_1 = 500 µm and the inside radius of curvature of the toolpath is R_2 = 140 µm. Therefore, the tangential velocity at the inside of the toolpath is $v_2 = (R_2/R_1)v_1$ = 40 µm/s. These conditions (φ = 0.05, v_2 = 40 µm/s) corresponds to the onset of disorder in Figure 2b.

The direct-write colloidal crystals exhibit structural colors that depend on the local crystalline order, lighting, and viewing conditions. The primary mechanisms by which structural colors are commonly created are broadly categorized into thin film interference, multilayer interference, grating diffraction, and other interference phenomena; each is enabled by nano- to micro- scale periodicity on the order of the wavelength of visible light.[26]

To characterize the light scattering and iridescence of a printed colloidal crystal, we illuminated the sample with collimated light such that the reflected light was projected onto the inside of a ping-pong ball, as illustrated in Figure 5c. This technique allows colors from all viewing angles to be visualized in a single image.[27] A sample with small grains (prepared at v = 610 µm/s with φ = 0.10) is shown in **Figure 4**a, and the corresponding color projection is displayed in Figure 4d. The separation of color leads us to hypothesize that the colloidal crystal acts as a reflective diffraction grating, because shorter wavelengths are diffracted at smaller angles with respect to the normal, as one would expect from the grating equation

$$m\lambda = d(\sin\theta_i + \sin\theta_r) \quad (2)$$

Where m is the diffraction order, d is the grating spacing, θ_i and θ_r are respectively the angles of incident and diffracted rays relative to the normal. In our experimental conditions, m = 1 since we observe only one diffraction order, θ_i = 0° since the incident ray is normal to the sample, and $d = \sqrt{3}/2D$ since the particles are arranged in a hexagonal lattice with center-to-center distance of D.

The colors on the hemispherical screen in Figure 4d can be linearly mapped with respect to polar angle θ and azimuthal angle ϕ, yielding Figure 4e. From Figure 4e, the radiant intensity can be averaged over all values of ϕ and plotted as a function of θ for each of the camera's three color channels, as shown in Figure 4f. The peaks can be used, in conjunction with Equation 2, to estimate particle size by using λ = 490, 550, and 650 nm as the peak wavelengths for the blue, green, and red channels respectively.[28] This yielded an estimated particle diameter of 751 nm, which matches the known colloid diameter of 746 ± 22 nm.

If there are many small colloidal crystal grains with different orientations present (such as for the sample shown in Figure 4a), each diffracting light toward a different azimuthal angle (ϕ), the scattered radiant intensity is almost constant along all azimuthal angles. However, if there are only a few grains present, distinct peaks are visible in the color projections. When the same experiment is performed with a large-grain sample (Figure 4b, prepared at v = 30 µm/s with φ = 0.025), distinct diffraction peaks are observed, as shown in Figure 4g and 4h. The six-fold symmetry of the diffraction pattern projected onto the sphere indicates that the particles assume a hexagonal arrangement.

Moreover, by analyzing the relative intensities of the peaks, it is possible to deduce information about the size proportions of the grains present in the illuminated region. To perform this analysis, we extracted the radiant intensity as a function of the azimuthal angle ϕ at a polar angle θ = 52° (see area marked in Figure 4h) and plotted the data as Figure 4i. Due to the six-fold symmetry of the diffraction pattern, the data is collapsed onto ϕ = 0 to ϕ = 60°. The highest and second-highest peaks should correspond to the largest and second-largest grains, which we designate as grains A and B, respectively. The radiant intensity level marked by the black solid line should then correspond to the much smaller grains of various orientations, which we designate as C. By comparing the relative peak intensities, we calculate that the area fraction of the various grain structures are $f_A = 0.41 \pm 0.14$, $f_B = 0.11 \pm 0.06$, and $f_C = 0.48 \pm 0.17$ (see SI for description of calculation). This result may be compared to the direct measurement of relative grain sizes via image analysis. An optical micrograph of the illuminated region is shown in Figure 4j, with the A, B, and C structures identified and labelled. By image segmentation, we measured $f_A = 0.32$, $f_B = 0.09$, and $f_C = 0.59$. Given the large uncertainty in the peak signal for A, the estimates from the diffraction peak intensities are in reasonable agreement with the measurements from the micrograph. Finally, using SEM (Figure 4k), we measured that grains A and B are misoriented by 19.5°. This is in close agreement with the radiant intensity plot (Figure 4i), which shows the A and B peaks 20° apart.

Sequential deposition of particles in multiple write passes, such as in overlapping or intersecting patterns, could facilitate the use of colloidal assembly for 3-D printing. However, we initially found that an overlap in the direct-write toolpath results in disorder, as shown in Figure 3b-ii. We hypothesize that this is due to the array of particles from the first pass being broken up by the liquid meniscus during the second pass. Therefore, if the particles from the first pass are effectively immobilized, then it may be possible to preserve crystallinity for multiple passes to build up 3-D prints.

One means of immobilizing the particle array is to sinter the particles. To sinter the particles, a colloidal crystal sample was heated to 110 °C for 15 minutes, followed by 1 minute of oxygen plasma treatment. The oxygen plasma improves the wettability of the surface, which becomes hydrophobic after the heating step. The sintering causes a slight color change in the colloidal crystal due to necks forming between the particles, which reduces the interparticle spacing. A second pass of direct-writing was then performed atop the first pass, as shown in Figure 3h. Separately, a second pass of direct-writing was also performed on a control sample which was not sintered, as shown in Figure 3g. The preservation of structural color on the sintered sample, compared to the whitish regions on the control sample, shows that sintering was effective in immobilizing the particle array from the first pass, allowing the particles on the second pass to self-assemble on the sintered array with crystalline registry. SEM confirms particle order on the second pass for the sintered sample (Figure 3i), and particle disorder on the second pass for the control sample (SI Figure S2). Potentially, layer-by-layer sintering (e.g., by in situ infrared heating) of the particles could be employed for building up multilayer structures with crystalline registry of the particles, which would be a means of 3-D printing colloidal crystals.

Additionally, we explore how the direct-write technique could be employed to assemble diverse colloidal assemblies with the potential for more functionality. As a simple example, in **Figure 5**, we demonstrate direct-writing of colloidal crystals comprising of different particle sizes (500 nm, 746 nm, and 1 μm) and different particle compositions (PS, PMMA, and silica) on the same silicon wafer. Figure 5 also demonstrates the limits to the width of the crystal that can controlled by the diameter of the needle. Although smaller needles may be used for direct-write assembly, the width of the crystal is not strictly proportional to the diameter of the needle, as shown from the progression of needle sizes from 22 gauge (OD, ID = 0.7, 0.4 mm) to 27 gauge (OD, ID = 0.4, 0.2 mm) to 33 gauge (OD, ID = 0.2, 0.1 mm). With the smallest needle size, 33 gauge, the crystal width was similar to that of the 27 gauge due to spontaneous spreading of the liquid meniscus that is difficult to control even at very low dispense rates (1.57 nL/s), as shown in SI Figure S3. Yet, spreading of the liquid meniscus at a finite contact angle is necessary for successful deposition of particles.[29,30] Future work on direct-writing of colloids could include exploring the technique's ultimate resolution limits by tuning the hydrophilicity of the surface via plasma treatment or predepositing molecular self-assembled monolayers onto the substrate to control spreading of the meniscus.

In conclusion, we demonstrated freeform fabrication of colloidal crystals by in-plane direct-write self-assembly, and experimentally derived an operational phase diagram, which maps write speeds and particle concentrations that lead to crystalline features. Furthermore, we investigated the effect of toolpath trajectory on the crystallinity of the colloidal assemblies, and showed that sintering can be used to stack overlapping passes. We also established grating diffraction as the mechanism for the structural color effects in these colloidal crystals, and showed that simple characterization of the optical properties of the crystals yields reliable information about microstructure, such as particle size, grain size, and orientation. In future work, in-plane direct-write assembly could be extended to a practical technique for 3-D printing of colloidal crystals if a means for rapidly sintering each layer could be developed. Finally, we note that, while macroscopic printed features can be well-controlled by the direct-write toolpath, at the microstructural level, every trace or image that is printed with direct-write is unique, which suggests applications of direct-write in generating patterns for use in optical encoding and security devices.

Experimental Section

Direct-write self-assembly: An aqueous suspension of polystyrene particles (750 nm diameter, Polysciences Inc.) was loaded into a 100 µl syringe (Hamilton 1710 RN) affixed with a blunt tip needle (Hamilton point style 3, 27ga) and placed into a custom-made holder. The plunger of the syringe is depressed using a linear actuator (M-229.26S, Physik Instrumente) commanded from a computer. The stage is heated to 30±0.1 °C by a thermoelectric chip (Custom Thermoelectric) and the stage temperature is measured by an embedded K-type thermocouple (Omega) fed to a temperature controller (PTC 10, Stanford Research Systems).

The stage is actuated by linear motors (Zaber LRM025A- E03T3-MC03) controlled by a two-axis stepper motor controller (Zaber X-MCB2- KX14B) via the Zaber Console software. To perform direct-write in complex trajectories, the shapes were drawn using Carbide Create software, and the G-code was converted into native motor commands using the G-code translator in the Zaber Console software.

Microstructural characterization: Optical images were taken using a Zeiss Smartzoom optical microscope. Images were taken in coaxial lighting mode (Fig. 1c, 2c, 2d, 2e, 5j) to clearly distinguish monolayers, bilayers, and multilayers. Images were taken in ring lighting mode (Fig. 3, 4, 5a, 5b) to clearly distinguish iridescent and non-iridescent regions. SEM was performed with a Zeiss Merlin High Resolution SEM in high efficiency secondary electron imaging mode, at an accelerating voltage of 1 kV and probe current of 100 pA. Image analysis was performed using ImageJ.

Characterization of optical properties: The colloidal crystal sample was illuminated by a light source (Ocean Optics HL-2000) directed by an optical fiber (Thorlabs M25L01, ø200μm, 0.22 NA) to a collimating lens (Thorlabs F230SMA-A, alignment wavelength = 543 nm, f = 4.34 mm, NA = 0.57). The collimated light was directed to shine through a hole drilled through a translucent hemispherical screen (half a ping pong ball) and onto the sample placed in the middle of the enclosing hemisphere. The light projected onto the screen was recorded with a DSLR camera (Canon EOS Rebel T3i) which was fixed in position using an articulated arm.

Supporting Information

Supporting Information is available from the Wiley Online Library or from the author.

Acknowledgements

The authors thank Dr. Justin Beroz for prior apparatus design and fabrication, and thank Cécile Chazot for helpful discussions regarding optics. Financial support for experiments was provided by a National Science Foundation CAREER Award (CMMI-1346638, to A.J.H.), and by the MIT-Skoltech Next Generation Program. A.T.L.T. was supported by a postgraduate fellowship from the Singapore Defence Science Organization. S.N. and M.K. were supported by the US Army Research Office through the Institute for Soldier Nanotechnologies at MIT, under contract number W911NF-13-D-0001 and by the National Science Foundation's CBET programme on "Particulate and Multiphase Processes" under grant numbers 1804241 and 1804092. E.C.D. was supported by the MIT Undergraduate Research Opportunities Program (UROP). J.T. was supported an SUTD international UROP award. J.K.W.Y. acknowledges funding from National Research Foundation Competitive Research Programme Grant No. CRP20-2017-0004. This work made use of the MRSEC Shared Experimental Facilities at MIT, supported by the National Science Foundation under award number DMR-14-19807.

Received: ((will be filled in by the editorial staff))
Revised: ((will be filled in by the editorial staff))
Published online: ((will be filled in by the editorial staff))

References

[1] S. Kinoshita, S. Yoshioka, *ChemPhysChem* **2005**, *6*, 1443.
[2] M. Kolle, U. Steiner, in *Encycl. Nanotechnol.*, Springer Netherlands, Dordrecht, **2019**, pp. 3840–3854.
[3] S. L. Burg, A. J. Parnell, *J. Phys. Condens. Matter* **2018**, *30*, 413001.
[4] Y. A. Vlasov, X. Z. Bo, J. C. Sturm, D. J. Norris, *Nature* **2001**, *414*, 289.
[5] N. D. Denkov, O. D. Velev, P. A. Kralchevsky, I. B. Ivanov, H. Yoshimura, K. Nagayama, *Nature* **1993**, *361*, 26.
[6] A. Van Blaaderen, R. Ruel, P. Wiltzius, *Nature* **1997**, *385*, 321.
[7] P. Jiang, J. F. Bertone, K. S. Hwang, V. L. Colvin, *Chem. Mater.* **1999**, *11*, 2132.
[8] Y. Xia, B. Gates, Y. Yin, Y. Lu, *Adv. Mater.* **2000**, *12*, 693.
[9] Y. Cui, M. T. Björk, J. A. Liddle, C. Sönnichsen, B. Boussert, A. P. Alivisatos, *Nano Lett.* **2004**, *4*, 1093.
[10] I. B. Burgess, L. Mishchenko, B. D. Hatton, M. Kolle, M. Lončar, J. Aizenberg, *J. Am. Chem. Soc.* **2011**, *133*, 12430.
[11] J. Hou, M. Li, Y. Song, *Angew. Chemie Int. Ed.* **2018**, *57*, 2544.
[12] Y. Yin, Y. Lu, B. Gates, Y. Xia, *J. Am. Chem. Soc.* **2001**, *123*, 8718.
[13] J. Park, J. Moon, H. Shin, D. Wang, M. Park, *J. Colloid Interface Sci.* **2006**, *298*, 713.
[14] J. Park, J. Moon, *Langmuir* **2006**, *22*, 3506.
[15] L. Wang, J. Wang, Y. Huang, M. Liu, M. Kuang, Y. Li, L. Jiang, Y. Song, *J. Mater. Chem.* **2012**, *22*, 21405.
[16] L. Cui, Y. Li, J. Wang, E. Tian, X. Zhang, Y. Zhang, Y. Song, L. Jiang, *J. Mater. Chem.* **2009**, *19*, 5499.
[17] H. Nam, K. Song, D. Ha, T. Kim, *Sci. Rep.* **2016**, *6*, 30885.
[18] J. Wang, L. Wang, Y. Song, L. Jiang, *J. Mater. Chem. C* **2013**, *1*, 6048.
[19] A. T. L. Tan, J. Beroz, M. Kolle, A. J. Hart, *Adv. Mater.* **2018**, *30*, 1803620.
[20] J. E. Smay, J. Cesarano, J. A. Lewis, *Langmuir* **2002**, *18*, 5429.
[21] J. A. Lewis, *Adv. Funct. Mater.* **2006**, *16*, 2193.
[22] M. Bedewy, J. Hu, A. J. Hart, in *2017 IEEE 17th Int. Conf. Nanotechnology, NANO 2017*, IEEE, **2017**, pp. 286–289.
[23] H. Cong, W. Cao, *Langmuir* **2004**, *20*, 8049.
[24] A. S. Dimitrov, K. Nagayama, *Langmuir* **1996**, *12*, 1303.
[25] B. G. Prevo, D. M. Kuncicky, O. D. Velev, *Colloids Surfaces A Physicochem. Eng.*

Asp. **2007**, *311*, 2.
[26] S. Kinoshita, S. Yoshioka, J. Miyazaki, *Reports Prog. Phys.* **2008**, *71*, 076401.
[27] A. E. Goodling, S. Nagelberg, B. Kaehr, C. H. Meredith, S. I. Cheon, A. P. Saunders, M. Kolle, L. D. Zarzar, *Nature* **2019**, *566*, 523.
[28] J. Deglint, F. Kazemzadeh, D. Cho, D. A. Clausi, A. Wong, *Sci. Rep.* **2016**, *6*, DOI 10.1038/srep28665.
[29] R. D. Deegan, O. Bakajin, T. F. Dupont, G. Huber, S. R. Nagel, T. a Witten, *Nature* **1997**, *389*, 827.
[30] R. Deegan, *Phys. Rev. E* **2000**, *61*, 475.

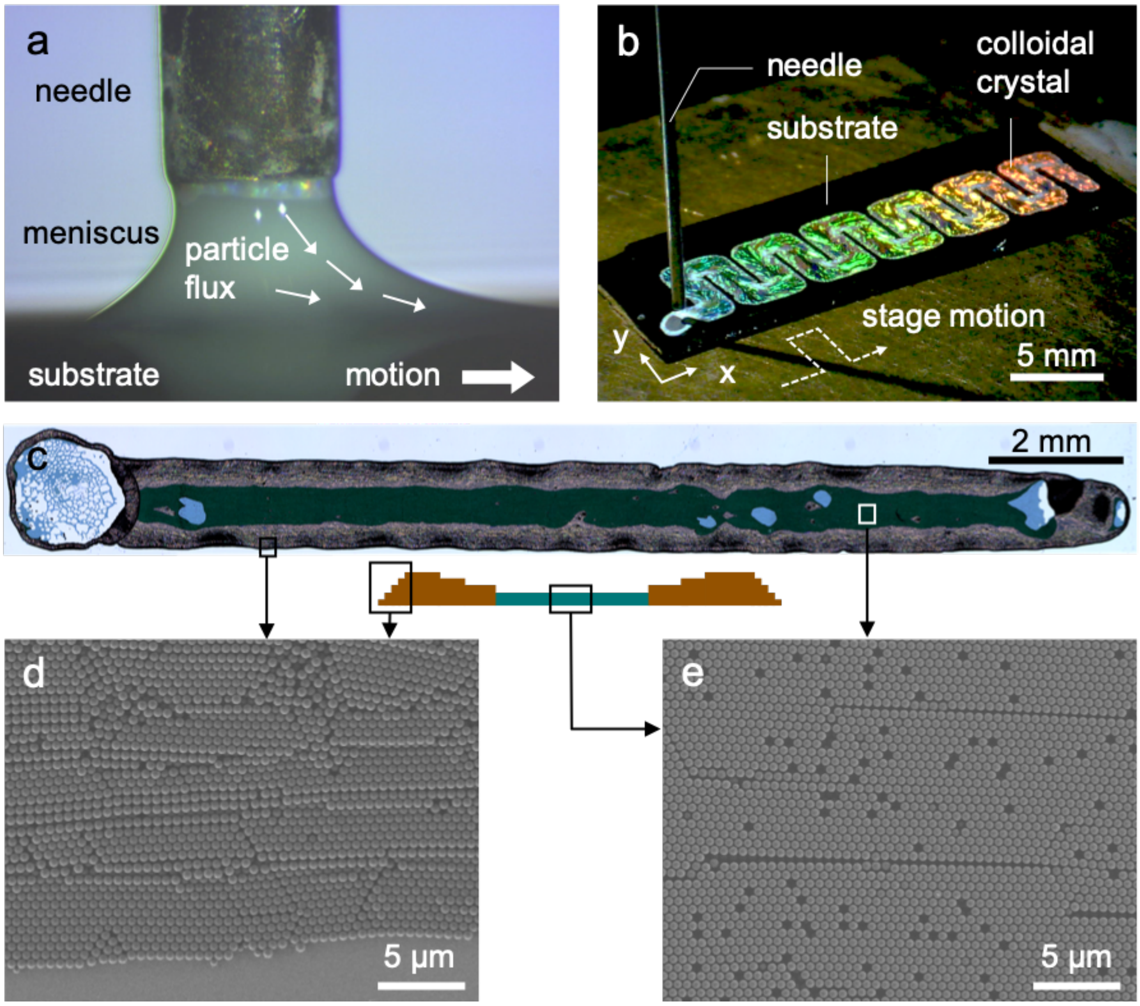

Figure 1. Fabrication of colloidal crystals by in-plane direct-write self-assembly. (a) In-plane direct-write self-assembly is performed by precision dispense of a colloidal suspension from a needle, coupled with lateral substrate motion. (b) A serpentine colloidal crystal is drawn by movement of the stage. (c) Optical image (top) and cross-section schematic (bottom) of an exemplary colloidal crystal trace. The edge of the crystal (brown coloration) is thicker than the middle. The middle consists of mostly particle bilayers (green coloration) and monolayers (blue coloration). (d) SEM image showing multilayer terraces at the edge of the crystal. (e) SEM image of the middle region of the crystal showing defects such as dislocations and vacancies.

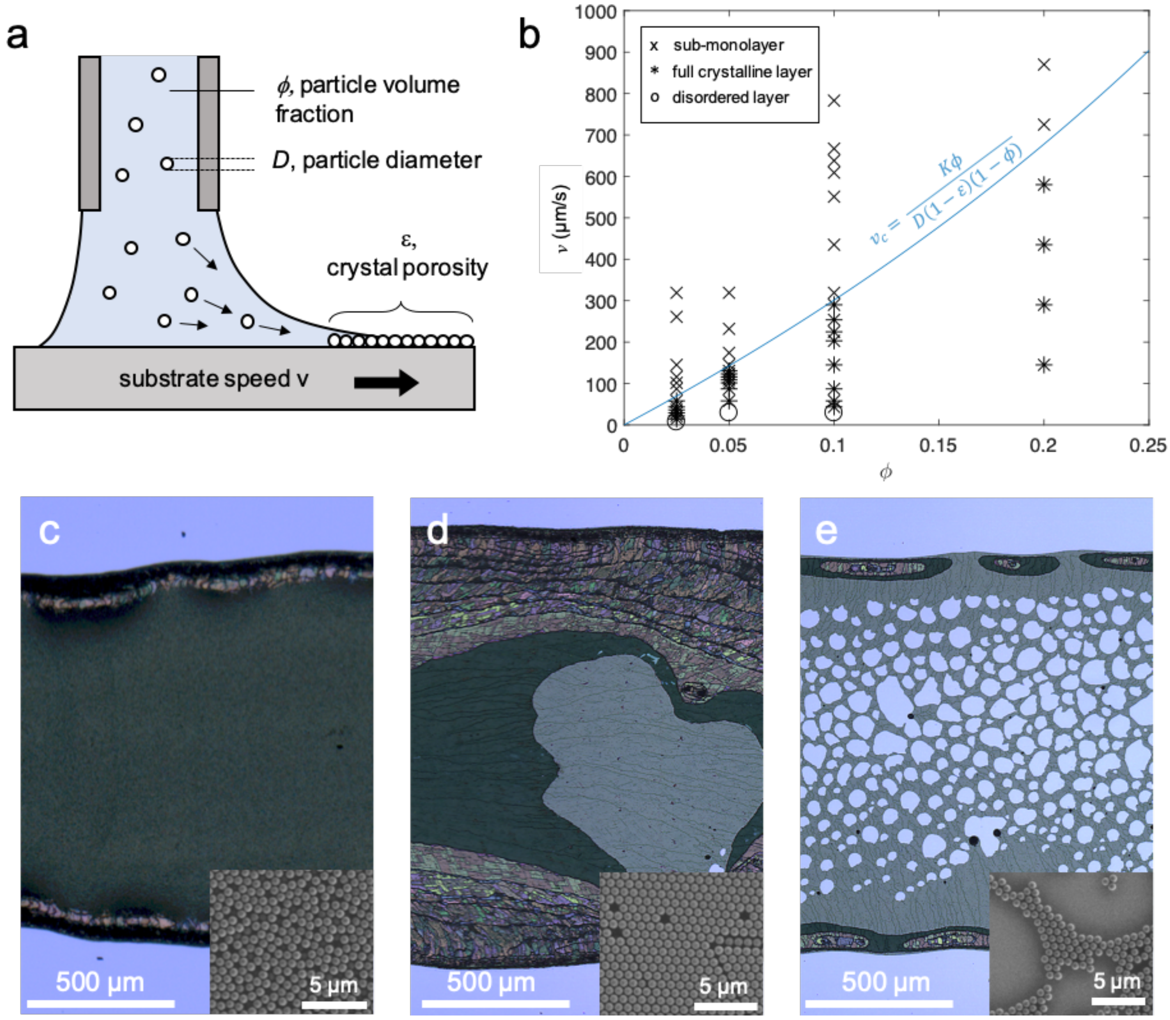

Figure 2. Optimization of direct-write process parameters to achieve well-packed crystalline deposits. (a) Schematic of the direct-write assembly process, where ϕ is the volume fraction of particles in solution, D is the particle diameter, ε is the porosity of the colloidal crystal, and v is the substrate speed. (b) An operational phase diagram where disordered, ordered, and sub-monolayer phases are plotted as a function of ϕ and v. The curve delineates the natural assembly speed as modelled by the Dimitrov-Nagayama equation with fitting parameter K. (c-e) Optical microscope images and inset SEM of colloid trails with (c) disordered, (d) ordered, and (e) sub-monolayer phases.

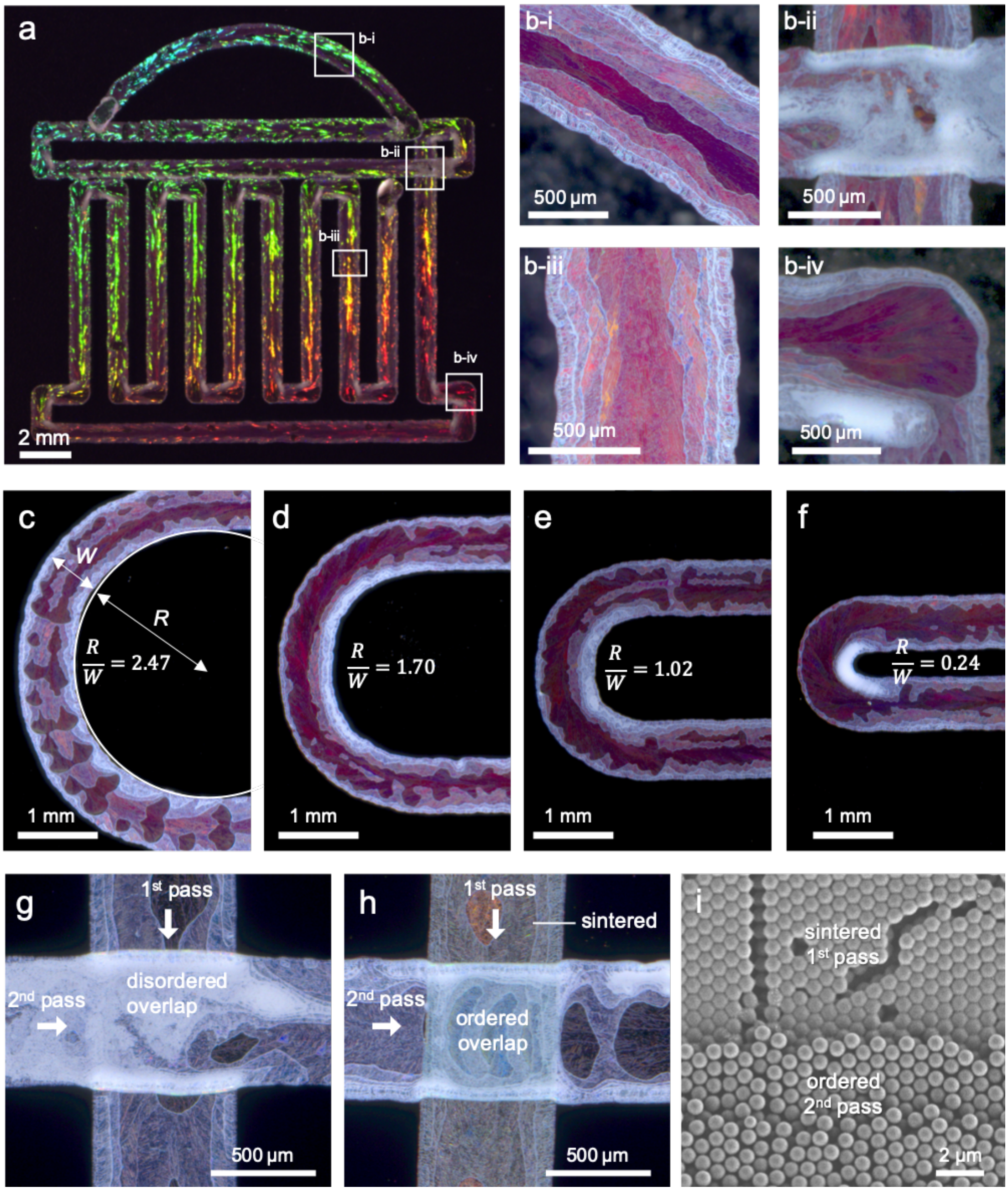

Figure 3. Effect of direct-write tool path on crystal order. (a) Photograph of a colloidal crystal patterned by control of the direct-write trajectory. (b) Optical microscope enlargements showing the morphology of a (b-i) wide arc, (b-ii) overlap, (b-iii) straight line, and (b-iv) sharp turn. (c-f) The crystallinity of a colloidal trail is affected by curvature of the direct-write trajectory, as demonstrated by trails with turning radius (R) of (c) 1.63 mm, (d) 1.12 mm, (e) 0.67 mm, and (f) 0.16 mm, and constant width $W = 0.66$ mm. Generally, the inside of the curved trail is ordered when $R/W > 1$ but becomes disordered when $R/W < 1$. (g-h) Optical images of perpendicular overlapping trails. (g) Without sintering, overlapping colloidal trails result in disorder, as apparent from the whitish region on the trail from the second pass. (h) After sintering of the trail from the first pass, the trail from the second pass is deposited atop with crystalline arrangement. (i) SEM image of a sintered first pass and an ordered second pass.

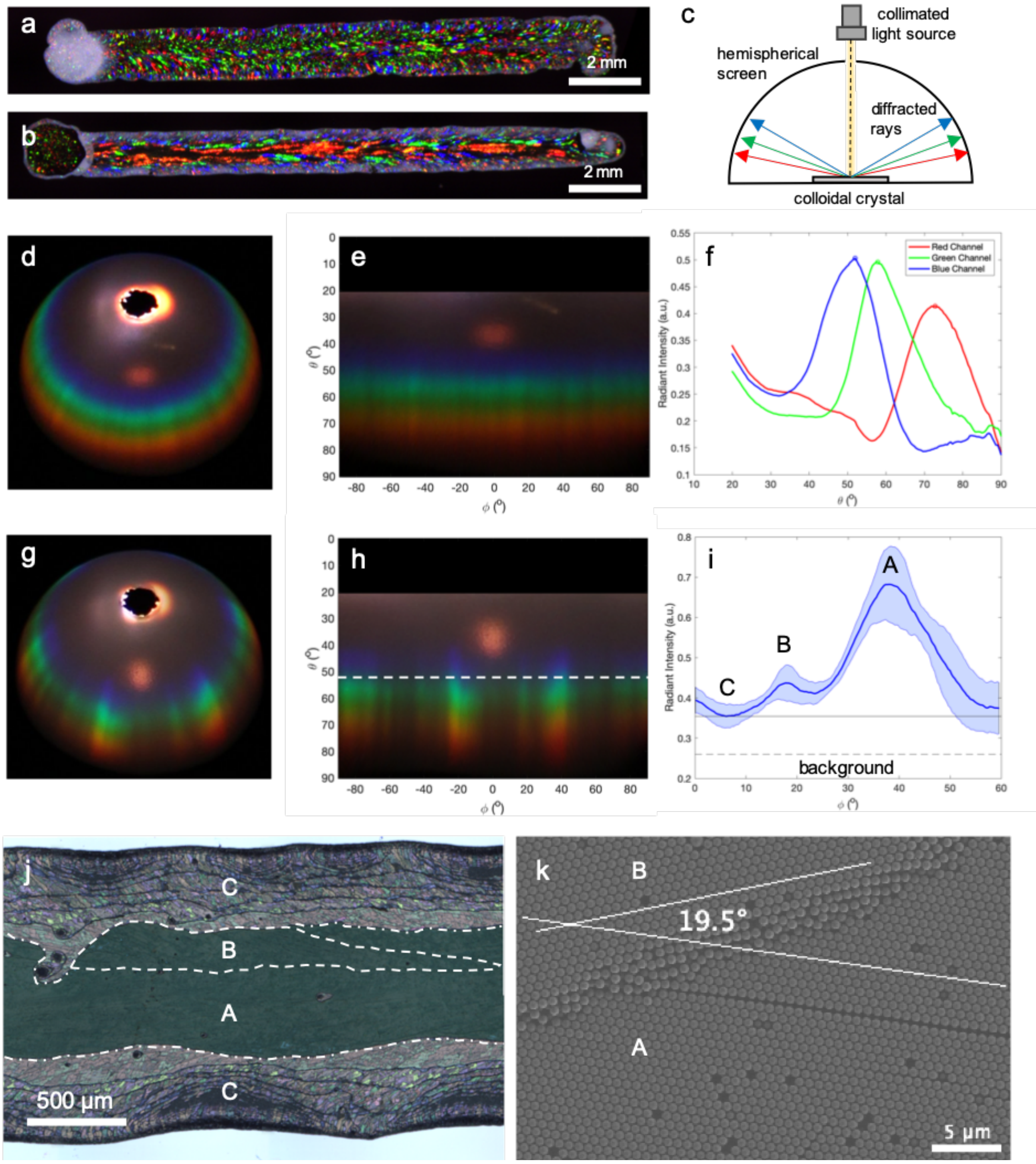

Figure 4. Optical properties of direct-write colloidal crystals. (a,b) Photographs of (a) small-grain and (b) large-grain colloidal crystal imaged under ring lighting around the objective lens. (c) Schematic depicting the characterization of optical properties by illuminating the colloidal crystal with collimated light at an angle normal to the crystal and observing the projection of diffracted colors on a hemispherical screen. (d,g) Photograph of colors projected from the (d) small-grain and (g) large-grain colloidal crystal. (e, h) Colors from the (e) small-grain and (h) large-grain samples linearly mapped onto azimuthal angle ϕ and polar angle θ. (f) Plot of radiant intensity vs θ for each of the RGB channels, obtained by averaging over all values of ϕ. (i) Plot of radiant intensity vs azimuthal angle ϕ derived from the blue channel of (h), ranging $\phi = 0$ to 60° averaged over the six fold symmetry regions, at θ = 52°. The solid blue line is the radiant intensity and the shaded region represents standard deviation. The highest peak is from the largest grain, A; the second highest peak is from the second-largest grain, B; and the lowest radiant intensity, denoted by the solid black line, is an

estimate of the amount of light from various other small grains, C. The dashed line represents the background illumination of the ping pong ball, measured in a non-colored region. (j) Optical image of the illuminated region, with A, B, and C grain structures identified. (k) SEM image analysis confirms that the largest grain A and the second-largest grain B are relatively orientated at 19.5°.

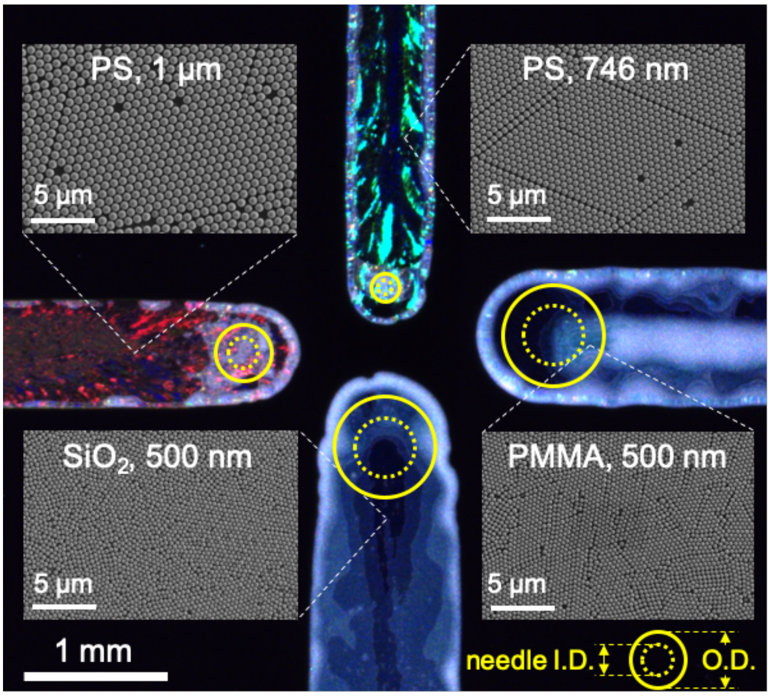

Figure 5. Direct-write fabrication of multiple colloidal materials on the same substrate. Clockwise from top: 746 nm polystyrene particles with a needle of OD, ID = 0.2, 0.1 mm; 500 nm polymethylmethacrylate (PMMA) particles with a needle of OD, ID = 0.7, 0.4 mm; 500 nm silica particles with a needle of OD, ID = 0.7, 0.4 mm; 746 nm polystyrene particles with a needle of OD, ID = 0.4, 0.2 mm. The needle diameters are overlaid on the respective colloidal crystal.

The table of contents entry should be 50−60 words long, and the first phrase should be bold.

Keywords: colloids, self-assembly, structural color, additive manufacturing, nanoparticles

A. T. L. Tan, S. Nagelberg, E. Chang-Davidson, J. Tan, J. K. W. Yang, M. Kolle, A. J. Hart*

In-Plane Direct-Write Assembly of Iridescent Colloidal Crystals

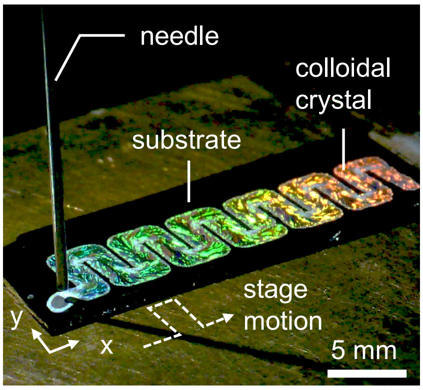

Direct-write is presented as a technique for fabricating high quality iridescent colloidal crystals directly from a digital template, without the need for masks or etching. The iridescence is characterized as a means for gaining feedback on grain size and orientation. By stacking multiple print passes, direct-write provides a pathway toward 3-D printing of colloidal crystals.

Supporting Information

In-Plane Direct-Write Assembly of Iridescent Colloidal Crystals

*Alvin T. L. Tan, Sara Nagelberg, Elizabeth Chang-Davidson, Joel Tan, Joel K. W. Yang, Mathias Kolle, A. John Hart**

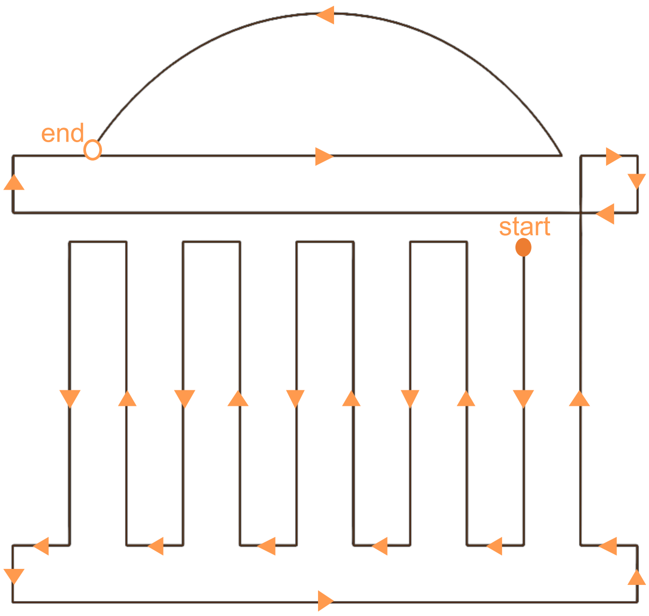

Figure S1. Simple vector graphic (black line) overlaid with the direct-write toolpath (orange arrows) used for fabrication of the colloidal crystal shown in Fig. 3a.

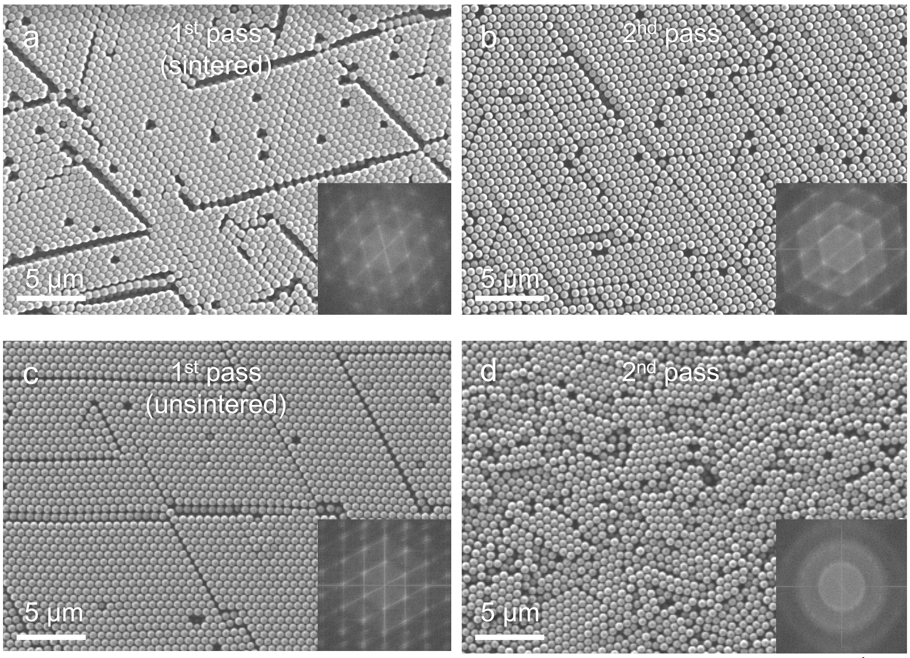

Figure S2. SEM of overlapping passes. (a) Sintered 1st pass. (b) 2nd pass over the sintered 1st pass. (c) Unsintered 1st pass. (c) 2nd pass over the unsintered 1st pass. Insets: 2-D Fast Fourier Transform of the corresponding image. Hexagonal peaks indicate order and the diffuse rings indicate disorder.

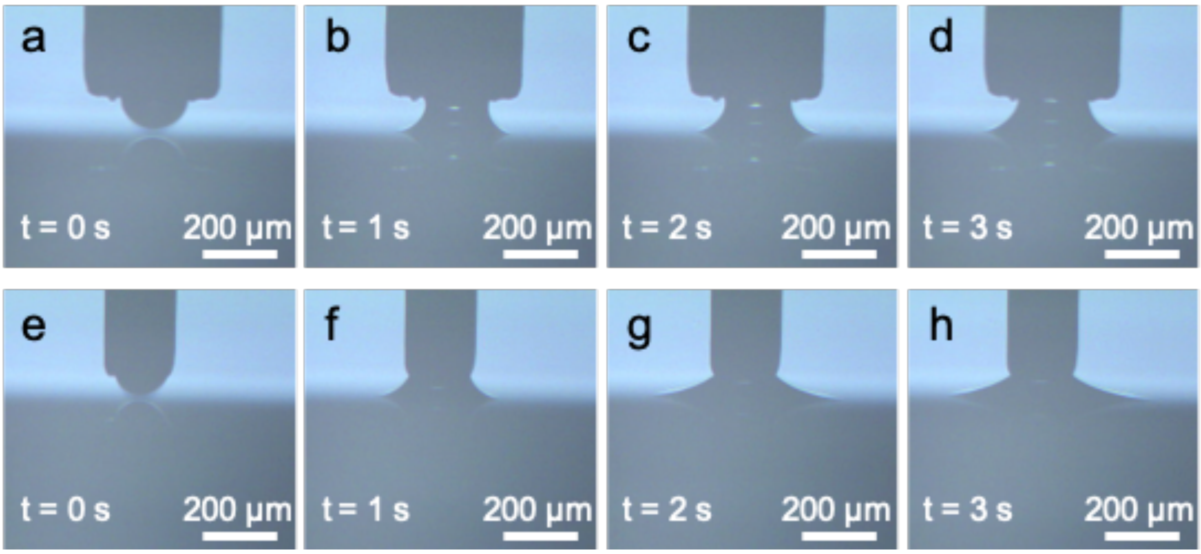

Figure S3. Optical video stills of the meniscus spreading from a 27 gauge needle (a-d) and a 33 gauge needle (e-h). In both cases, the dispense rate is the same (1.57 nL/s). The meniscus spreads quickly from the 33 gauge needle beyond the radius of the needle, thus making the width of the colloidal trace hard to control.

Quantitative Angle Measurements from Ping Pong Ball images.

The ping pong ball as a screen is a clean and simple way of capturing the full color distribution for all viewing angles in just one measurement. From a top view of the ping pong ball it is simple to quantitatively map pixels on the image to precise angles (θ, ϕ). From the center of the ping pong ball (found by manually fitting a circle to the edges using ImageJ)

$$(x, y) = (R\cos(\phi)\sin(\theta), R\sin(\phi)\sin(\theta))$$

Unfortunately, an unobstructed top view of the ping pong ball is not always easily captured, particularly when the illumination is at normal incidence. For this reason, we captured the color pattern from a side view of the ping pong ball. We define the viewing direction of the camera as $(\theta_{cam}, \phi_{cam})$ and mapping back from this view to the global coordinates (θ, ϕ) can be done with a coordinate transformation. First, we define a new pair of angles (Δ, γ) measured from the camera to sample axis as shown in Figure S4. Again, measured from the center of the ping pong ball the pixel locations corresponding to these angles are:

$$(x, y) = (R\cos(\gamma)\sin(\Delta), R\sin(\gamma)\sin(\Delta))$$

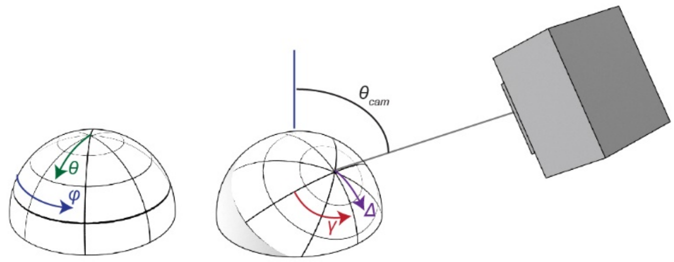

Figure S4. Camera Angle. Global coordinate system (θ, ϕ) shown as well as the projected system, when imaged at an angle θ_{cam}. Δ is the angle measured from the camera axis, and γ is the azimuthal angle in this rotated coordinate system. By converting from (Δ, γ) coordinates to the global (θ, ϕ) coordinates, we can quantitatively determine the angle to which each color is scattered from photographs taken at an angle.

In order to determine (Δ, γ) in terms of (θ, ϕ), consider a point on the surface of the ping pong ball in 3D:

$$\begin{pmatrix} X \\ Y \\ Z \end{pmatrix} = \begin{pmatrix} \cos(\phi)\sin(\theta) \\ \sin(\phi)\sin(\theta) \\ \cos(\theta) \end{pmatrix}$$

We then can rotate these coordinates first around the Z-axis by ϕ_{cam} then around the y axis by θ_{cam} to get new coordinates:

$$\begin{pmatrix} X' \\ Y' \\ Z' \end{pmatrix} = \begin{pmatrix} \cos(\theta_{\text{cam}}) & 0 & \sin(\theta_{\text{cam}}) \\ 0 & 1 & 0 \\ -\sin(\theta_{\text{cam}}) & 0 & \cos(\theta_{\text{cam}}) \end{pmatrix} \begin{pmatrix} \cos(\phi_{\text{cam}}) & -\sin(\phi_{\text{cam}}) & 0 \\ \sin(\phi_{\text{cam}}) & \cos(\phi_{\text{cam}}) & 0 \\ 0 & 0 & 1 \end{pmatrix} \begin{pmatrix} X \\ Y \\ Z \end{pmatrix}$$

And then:

$$\beta = \text{atan}\left(\frac{Y'}{X'}\right), \qquad \Delta = \text{acos}\, Z'$$

Grain and Colloid Size Estimates

From the color distributions, it is possible to gain an estimate of the grain and colloid size in the illuminated area. Each grain will diffract light in a pattern with six-fold symmetry, the angle that each color is scattered to is set by the first order diffraction equation:

$$\sin(\theta) = \frac{\lambda}{d},$$

where $d = \frac{\sqrt{3}}{2}D$ is the distance between lattice planes and D is the diameter of the colloids. Figure 4f in the main part of the manuscript shows the radiant intensity as a function of polar angle θ for each of the three color channels, obtained by averaging over all values of ϕ. The peaks can be used to estimate colloid size, by using $\lambda = 490$nm, 550nm, and 650nm as the peak wavelengths for the blue, green, and red channels respectively.[1] This yielded an estimated diameter of 751nm whereas the real colloid size was 747nm.

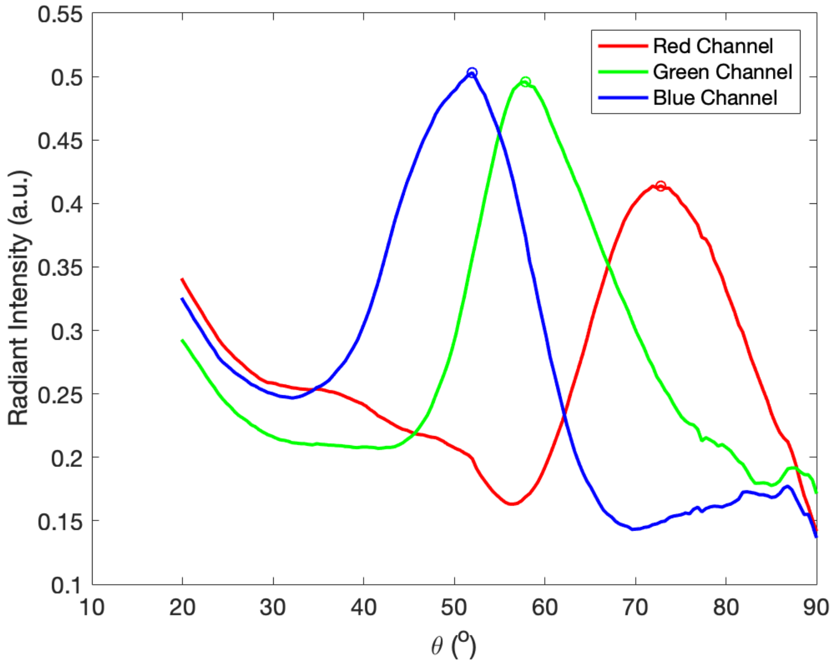

Figure S5. Polar angle dependence of the radiant intensity of diffracted light for the camera's three color channels. Radiant intensity measured from ping pong ball photographs for each of the RGB channels. The peak values can be used to determine colloid size.

More interestingly, the spacing and relative height of diffraction orders in the azimuthal direction gives an estimate of the grain structure. If there are many small grains present, then there will be many individual diffraction patterns with different azimuthal orientations, such that the overall scattered radiant intensity is constant as the azimuthal angle ϕ is varied. If there are only a few grains present, however, distinct peaks are visible in Figure 4g.

In order to get an estimate of the size of the grains using this technique, we compare the relative radiant intensity of each of the peaks. Because of the six-fold symmetry of the colloidal crystal structure, we only need to look at an azimuthal angle range of 60º of the scattered light; therefore we average each of the 60º sections that is visible in our image of the ping pong ball (Figure S6a and b). Because scattering from the ping pong ball is not perfectly uniform, a white scatterer (Teflon tape) was used to normalize the azimuthal color distributions. The Teflon tape acts a Lambertian scatterer and should not be used to normalize in the polar direction, as its scattering profile does have a θ dependence.

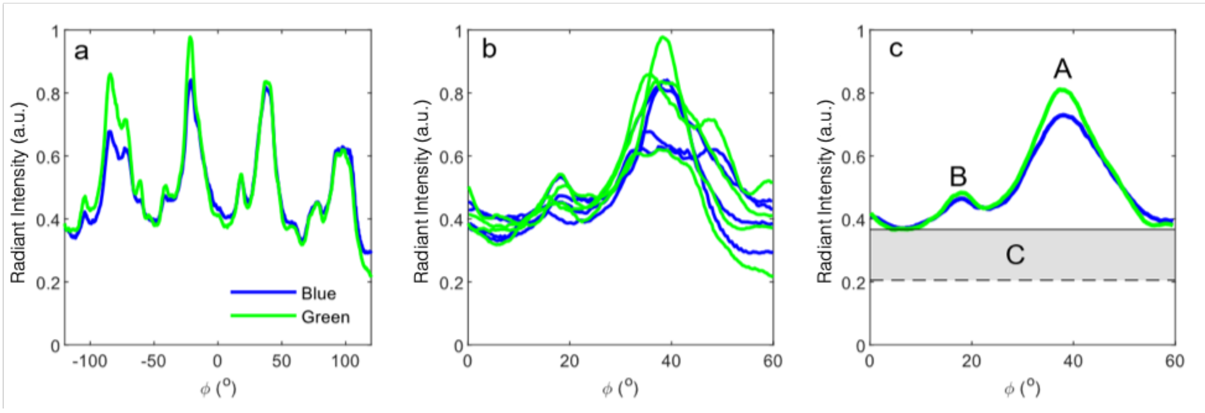

Figure S6. Azimuthal Dependence of Diffracted light. Radiant intensity measured in the color projection at polar angles θ, where peak radiant intensity was observed (see Figure S5). **a)** Radiant intensity of the color projection for the full azimuthal range in the green and blue channel. **b)** The data in (a) folded back over each 60º section. **c)** The average of (b), showing two distinct peaks in radiant intensity corresponding to two large grains. The dashed line represents the background illumination of the ping pong ball, and the solid line represents the minimum corresponding to small randomly oriented grains.

In the case of the example shown in Figure S6, there are two distinct peaks, as well as a low level continuum of diffraction from small grains. We first subtract off the background that can be associated with the illumination of the ping pong ball (dotted line in Figure S6c). The integral of the area under the curve corresponds to the total light scattered by the printed crystal. The area labeled as C corresponds to light scattered by small randomly oriented smaller grains. A and B correspond to larger grains. The relative height of A and B should correspond to the relative size of these two grains. The uncertainty is estimated from the standard deviation of the different 60º sections.

From this information, we can estimate that there is a large grain (A) that covers $41\% \pm 14\%$ of the illuminated area, a smaller grain (B), rotated about 20^o from the first, that covers $11\% \pm 6\%$ of the illuminated area, and the remaining $48\% \pm 17\%$ is covered by small, randomly oriented grains, which corresponds with observations from optical and SEM images, as shown in Figure 4j,k in the main text.

References

[1] J. Deglint, F. Kazemzadeh, D. Cho, D. A. Clausi, A. Wong, *Sci. Rep.* **2016**, *6*, DOI 10.1038/srep28665.